DOI: 10.1002/zaac.201000124

Transmission Electron Microscopy Study of Copper Containing Spinel-type In_2S_3 Nanocrystals Prepared by Rapid Pyrolysis of a Single Molecular Precursor

Enrique Quiroga-González,[a] Wolfgang Bensch,[a] Viola Duppel,[b] and Lorenz Kienle*[c]

Keywords: Indium; Copper; Nanocrystals; Pyrolysis; Single precursor; Electron microscopy

Abstract. Copper containing spinel-type In_2S_3 nanocrystals were prepared by rapid pyrolysis (RP) from a single source inorganic-organic hybrid molecular precursor with an initial Cu:In:S ratio of 1:9:16.5. The precursor was synthesized in a one-step hydrothermal reaction with high yield. After a treatment of the precursor for 10 s at 1000 °C a powdered material was obtained. The X-ray powder pattern exhibits broad reflections indicative for the spinel-type and crystallites in the nanometer range, however, the positions of the reflections match well with different compounds of the In-S and Cu-In-S systems.
High resolution transmission electron microscopy (HRTEM) studies in connection with EDX analyses evidence the presence of cubic spinel-type copper containing In_2S_3. Two such In_2S_3 phases coexist with one being copper poor and the other having a larger copper content. The coexistence of these two compounds is reflected by the Raman and UV/Vis spectra.

1 Introduction

Semiconducting materials at the nanoscale are of great interest because they offer a rich palette of optical, electronic, and catalytic properties, which can be tuned by particles' size and shape [1, 2]. Such scenario is well known for In_2S_3 nanoparticles [2]. This compound is polymorphic and can crystallize either in the α, β or γ structures [3–6]. The structures of the α and β phases can be described as spinel-like. But contrary to a normal spinel structure, one third of the tetrahedral sites remains empty, which leads to the quasi-quaternary compound with formula: $[In_2]_O[In_{2/3}h_{1/3}]_TS_4$ (h represents the vacant sites and T and O represent the tetrahedral and octahedral sites, respectively) [5]. The α modification is stable above 420 °C and has a cubic structure (space group $Fd\bar{3}m$, a_α = 1.077 nm). Below that temperature the material transforms into the tetragonal β-In_2S_3 due to the ordering of the vacancies. The cell parameters of this structure are $c_\beta \sim 3c_\alpha$ = 3.2322 nm, and $a_\beta \sim a_\alpha/(2)^{1/2}$ = 0.7619 nm (space group $I4_1/amd$). Nevertheless if In_2S_3 is prepared with an excess of In larger than 0.5 % the α modification is stable even at room temperature [6]. Above 754 °C all indium atoms occupy octahedral interstices of the close-packed sulfur sublattice, forming the trigonal γ-In_2S_3 [3, 4]. This structural modification is stable at room temperature if ca. 5 at-% of the elements arsenic or antimony are incorporated in the structure.

In_2S_3 may replace the toxic CdS buffer layer in high efficient solar cells [7–13]. This material is also of importance due to its photoluminescent (PL) properties, which are enhanced for crystallites with reduced sizes [14]. Nanoparticles of In_2S_3 could emit green light produced by band to band transitions [14–16], blue light coming from deep trap states [2] and orange light due to interstitial indium defects [16]. The defect chemistry of In_2S_3 is of importance for the PL properties as was shown in [17]. Additionally other applications like degradation of organic pollutants under visible light irradiation were reported [18]. Nanocrystalline cubic and tetragonal In_2S_3 were prepared by applying a wide range of methods like hydrothermal synthesis [19], solution reactions [1, 16], pyrolysis of molecular compounds [20], among others, which lead to particles with a variety of morphologies.

The crystal structure of α- or β-In_2S_3 presents a large amount of vacancies that can serve as host for a number of metal ions to form semiconducting and/or magnetic materials [21]. This structural and chemical speciality distinguishes it from II–VI compounds, which tend to expel guest ions [1]. Very recently, it has been reported that the effective optical band gap of In_2S_3 decreases upon incorporation of copper shifting the density of states to the near infrared [5]. This example of band engineering allows the use of this material as active layer in solar cells and photodetectors. Actually, a high-sensitivity (photon-to-electron gain > 40), high-speed (video-frame-rate-compatible) photoconductive photodetector based on copper-doped In_2S_3 was reported [22]. The material was synthesized by a solution

* Prof. Dr. L. Kienle
E-Mail: lk@tf.uni-kiel.de
[a] Institute for Inorganic Chemistry
Christian-Albrechts-University Kiel
Max-Eyth Str. 2
24118 Kiel, Germany
[b] Max Planck Institute for Solid State Research
Heisenbergstraße 1
70569 Stuttgart, Germany
[c] Institute for Material Science
Christian-Albrechts-University Kiel
Kaiserstr. 2
24143 Kiel, Germany

route using butylamine and oleylamine as solvents. Another possible approach for the preparation of such nanocrystalline compounds is the use of single molecular precursors [20, 23, 24]. But until now copper-doped In_2S_3 nanocrystals were not fabricated in this way. The search for suitable precursors and their applications is a topic of intense actual research because the elements of interest are homogeneously distributed in the precursor. A variety of fabrication methods that use molecular single sources were studied, ranging from chemical vapor deposition (CVD) [23] to simple pyrolysis [20] or spray pyrolysis [24]. In these studies compounds like metallic thiocarboxylates or other indium complexes like $[MeIn(SCH_2CH_2S)]_n$ were applied. An interesting class of molecular precursors could also be the indium containing inorganic-organic hybrid open framework compounds, which have been reported recently [25, 26]. These materials are promising candidates for the synthesis of nanocrystalline products because they are composed of clusters with nanometric dimensions and they can be obtained with a variety of metal cations and with different compositions. Furthermore, the samples can be prepared by a simple one-pot synthesis method and they are obtained in high yields. To the best of our knowledge, the potential of these materials as single source precursors for the preparation of nanostructures was not explored until now.

Here we report first results of the preparation of copper containing In_2S_3 nanocrystals obtained by heating the single source precursor $(C_{13}H_{28}N_2)_5[Cu_2In_{18}S_{33}]\cdot xH_2O$ ($x \sim 17$) containing copper and indium in 1:9 ratio. The products were synthesized by heating the starting material for only a few seconds (rapid pyrolysis, RP). Such a low Cu:In ratio enhances the chance for doping of In_2S_3 rather than for formation of a stoichiometric Cu-In-S compound. The method presented here is easy, fast, and does not require elaborated equipment. A detailed microstructural analysis with high resolution transmission electron microscopy evidences the formation of two In_2S_3 phases containing different amounts of copper.

2 Experimental Section

2.1 Preparation of the Precursor

A hybrid (organic-inorganic) Cu-In open framework thiometalate with composition $(C_{13}H_{28}N_2)_5[Cu_2In_{18}S_{33}]\cdot xH_2O$ ($x \sim 17$) (**1**), which is isostructural to the known framework with composition $(C_{13}H_{28}N_2)_5[Cd_4In_{16}S_{33}]$ [26], was prepared using CuS (0.7 mmol, 99 %, Aldrich), indium (4.2 mmol), sulfur (6.9 mmol) and 4,4'-trimethylenedipiperidine (13.46 mmol). The precursors were mixed with water (2.5 mL) and ethylene glycol (2.5 mL) in a 35 mL teflon-lined stainless steel autoclave and stirred for 15 min. The sealed vessel was then heated at 190 °C for 5 days. After cooling to room temperature, the product was filtered and washed with water, ethanol, and acetone. Prismatic yellow crystals in a yield larger than 90 % based on indium were obtained. The crystal structure of **1** is composed of corner-linked T4 supertetrahedral clusters, with the two Cu^+ cations occupying two of the four positions around the central tetrahedral sulfur site. Further structural details can be found in [26]. The chemical composition of **1** was determined with C-H-N-S analysis and AAS.

2.2 Preparation of the Nanocrystals

The product (100 mg) was crushed and the obtained powder was introduced in quartz ampoules, which were evacuated and sealed. The ampoules were afterwards introduced in an oven pre-heated at 1000 °C for 5 and 10 s respectively, from which brown (**RP5**) and black (**RP10**) particles were obtained. An additional experiment was performed heating the material for 60 s (**RP60**) to test whether the amount of carbon can be reduced by a prolonged treatment. Additionally, structural changes induced by the longer heating times can be analyzed. The experiments were performed several times and the results of the analyses demonstrate the high reproducibility of the preparation method. According to EDX analyses, the obtained powders have the same Cu:In:S ratio as the precursor with slight variations typical for the EDX method. Elemental C-H-N analysis for **RP5**: C, 15.43; H, 2.56; N, 2.60 wt.-%. For **RP10**: C, 7.79; H, 0.57; N, 1.02 wt.-%. For **RP60**: C, 7.77; H, 0; N, 0.86 wt.-%. For **1**: C, 16.22; H, 3.03; N, 3.14 wt.-%.

2.3 Characterization Methods

For high resolution transmission electron microscopy, HRTEM (Philips CM 30ST, LaB_6 cathode, 300 kV, Cs = 1.15 mm), the samples **1**, **RP5** and **RP10** were crushed and the resulting micro-particulates were transferred to carbon/aluminum grids. SAED (selected area electron diffraction) and PED (precession electron diffraction) [27, 28] were carried out using a diaphragm that limited the diffraction to a circular area of 2500 Å in diameter. All HRTEM micrographs were evaluated (including Fourier filtering) with the programs Digital Micrograph 3.6.1 (Gatan) or Crisp (Calidris). Chemical analyses by EDX were performed in the scanning and nanoprobe mode of the CM30ST instrument using a Si/Li-EDX detector (Noran, Vantage System).

X-ray powder diffraction was performed with a STOE STADI-P diffractometer in transmission mode using a position sensitive detector and Ge monochromated Cu-$K_{\alpha 1}$ radiation (λ = 1.54056 Å).

The Raman measurements were performed with a Dilor X-Y Raman spectrometer. For this purpose an Ar-Kr Laser RA2018 of Spectra Physics working in the range of 454.5 to 647.1 nm was used. The 488 nm line was selected, and the laser power was limited to approximately 10 mW in order to avoid artefacts in the measurements due to heating.

Measurements of optical reflection were carried with a Cary 5000 UV/Vis/NIR spectrophotometer. The instrument uses a tungsten halogen lamp and a photomultiplier as light source and detector respectively in the range of 200–850 nm. In the range 850 to 3300 nm a deuterium lamp as light source and a cooled lead sulfide cell as detector are used.

3 Results and Discussion

3.1 X-ray Powder Diffraction

Figure 1 shows the X-ray powder diffractograms of the different materials. Obviously, the parent material **1** is transformed after the very short heat treatment yielding a sample with a very low crystallinity (**RP5**). An increase in the reaction time to 10 s leads to a new crystalline material (**RP10**). The positions of the reflections of this material indicate a relatively small unit cell, and the broadness of the reflections indicates the nanocrystalline nature of this material. The size of coherent scattering domains of **RP10** was calculated from the full-width

Zeitschrift für anorganische und allgemeine Chemie ZAAC Journal of Inorganic and General Chemistry

at half-maximum (FWHM) of the most intense reflection at around 27.6° 2θ applying the Scherrer formula yielding about 15 nm (no correction for instrumental broadening). The powder pattern of the sample annealed for 60 s (not shown) presents the same reflections which are now slightly sharper. The size of the crystals of this sample is about 28 nm, i.e., annealing for a longer time leads to a growth of the coherently scattering domains, however, the amount of carbon is not significantly reduced by this heat treatment (Experimental Section).

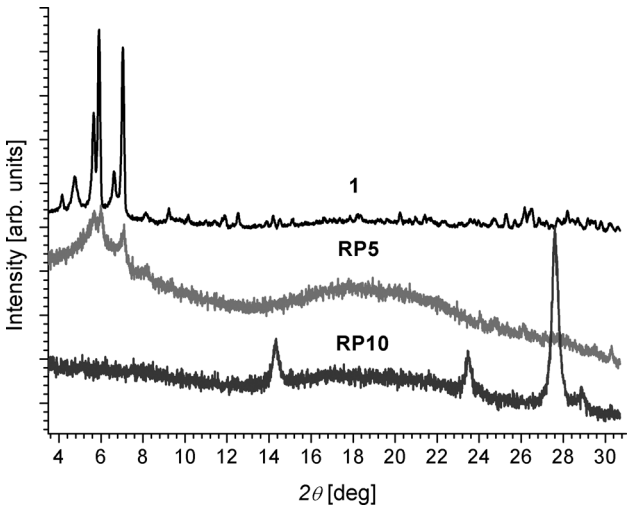

Figure 1. X-ray powder diffractograms of the different samples. It can be observed that **1** reduces its crystallinity upon annealing time (**RP5**) to finally crystallize forming a new material (**RP10**).

A detailed analysis of the positions of the reflections in the powder pattern of the nanocrystalline material **RP10** shows a good match with those of α-In_2S_3 [29], β-In_2S_3 [30], and $CuIn_5S_8$ [31] (Figure 2). However, due to the broadening of the reflections a definite decision about the structure of the nanocrystals of **RP10** cannot be made. We note that there is some confusion in literature concerning the α- and β-modifications of In_2S_3 with respect to the correct space group. Most authors use the tetragonal space group $I4_1/amd$ for β-In_2S_3 and the cubic space group $Fd\bar{3}m$ for α-In_2S_3. There is one crystallographic study where cubic symmetry ($Fd\bar{3}m$) was observed for nonstoichiometric In_2S_3 whereas the tetragonal superstructure was found for the stoichiometric sample [32]. In any case the differences of the powder patterns of the two modifications are very small and the tetragonal indium sulfide could only be identified due to the presence of weak superstructure reflections. The present material consists of nanosized crystallites and despite a very long acquisition time the powder pattern does not show any reflection indicative for the presence of tetragonal In_2S_3. This is in full agreement with electron diffraction (see below) where also no superstructure reflections could be observed. The situation becomes more complex assuming the presence of small amounts of $CuIn_5S_8$ (space group $F\bar{4}3m$) or the cubic variant crystallizing in $Fd\bar{3}m$ reported recently for $NaIn_5S_8$ [33]. To illustrate the difficulty to assign a distinct phase in the experimental powder pattern, an X-ray diffractogram was calculated containing the reflections of α-In_2S_3, β-In_2S_3, and $CuIn_5S_8$ with the two different space groups (cf. Figure 2). For the calculated reflection profiles the FWHM of the experimental pattern was used. The comparison to the experimental pattern evidences the difficulty of a definite phase assignment.

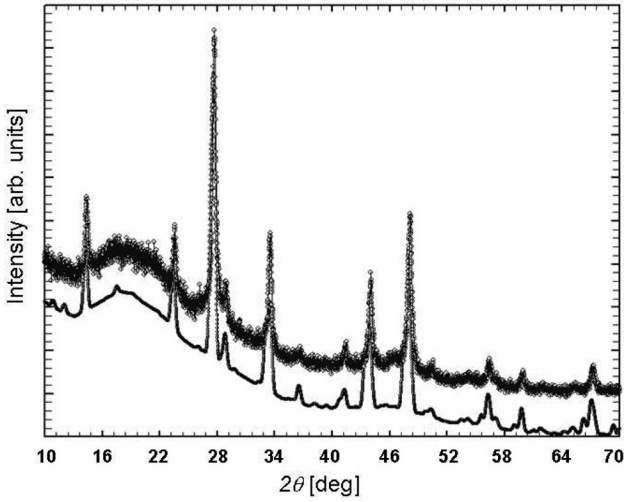

Figure 2. Top trace: experimental powder pattern of sample **RP10**; bottom trace: simulated powder pattern containing the reflections of α-In_2S_3, β-In_2S_3, and of $CuIn_5S_8$. The experimental pattern is shifted for clarity.

In addition, recent reports mentioned that there is a transition from the tetragonal space group of β-In_2S_3 (the most common room temperature modification) to cubic symmetry when In is partially replaced with a metal cation like Cu^+ or Na^+ at different levels [33, 34], which yield compounds with formula $[In_{16}]_O[In_{5.23-x/3}M_xh_{2.67-2x/3}]_TS_{32}$ where M is the substituting metal. The maximum substitution level is $x = 4$, resulting in a compound with formula MIn_5S_8 [5]. In the present case the cubic modification is most likely due to the presence of small amounts of copper (see also below). Because the analysis of the X-ray powder pattern gives no clear picture about the constituents in the material **RP10**, a TEM analysis was performed.

3.2 Transmission Electron Microscopy Investigations

3.2.1 The Precursor Material

The samples of this material contain two components with distinct chemical composition and structure. The first component (**W**) consists of strongly disordered crystals as evidenced by HRTEM and electron diffraction patterns, cf. Figure 3a. The disordering is based on layered structural motifs as verified by the diffuse streaks seen in FFTs of high resolution micrographs and the electron diffraction pattern (see inset in Figure 3a). EDX analysis identifies **W** as a binary phase In-S with an atomic ratio close to In:S ~ 2:3. The characteristic high d values, e.g. $d = 9.42$ Å calculated from the diffraction pattern of Figure 3a, indicate that the present structure can not be assigned to one of the known binary bulk phases. The second and most abundant component (**X**) is a ternary phase of the

Cu-In-S system with a stoichiometry close to the specified nominal composition of the precursor, i.e. $Cu_2In_{18}S_{33}$ when neglecting the molecular constituents. The average of four EDX point analyses performed on distinct particles gave an atomic ratio Cu:In:S = 6.12 (0.78) : 32.46 (0.95) : 61.42 (1.35) compared to 3.7:33.9:62.2 for $Cu_2In_{18}S_{33}$ (**1**). As demonstrated by HRTEM and electron diffraction (Figure 3b) the particles are amorphous even without significant structural ordering inside nanoscale areas. According to the X-ray powder pattern the starting material **1** is crystalline in the as prepared state and no hints are seen for the presence of In_2S_3. One possible explanation for the present observation is that **1** is partially decomposed under ultra high vacuum conditions and just after switching of the electron beam some material crystallized (component **W**).

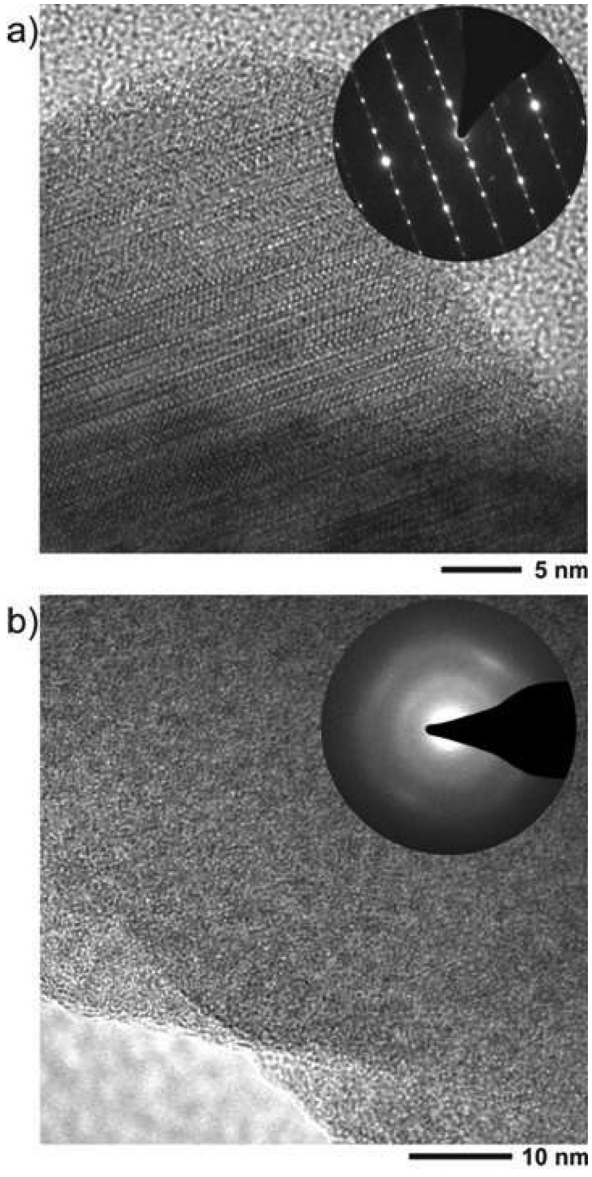

Figure 3. HRTEM micrographs and electron diffraction patterns (inset) of the components **W** (a) and **X** (b).

Taking the amorphous chalcogenide based phase change materials [35] as examples, we checked whether the degree of structural ordering in **X** changes under the influence of electron beam impact, particularly whether crystallization occurs [36].

When irradiating **X** for a long-term with the dose usually applied for HRTEM no changes of the amorphous structure can be detected. However, a massive dose with an increase of the current density by factor 40 compared to the normal value can be adjusted by removing the condenser aperture. Under such conditions crystalline nanoparticles were evaporated from the amorphous precursor (cf. Figure 4), while the remaining target material for electron bombardment stays amorphous. Closer inspection shows that the diameter of the nanoparticles is determined by the distance from the high dose irradiation area of the precursor (see Figure 4). Next to these areas a percolation of larger particles is observed, whereas more and more separated and smaller particles occur with increasing distance (see insets in Figure 4). Generally, the particle sizes appear uniform inside areas with the same distance from the area irradiated with high dose, e.g. for large distances of several microns reduced sizes of nanoparticles below 2 nm are dominant.

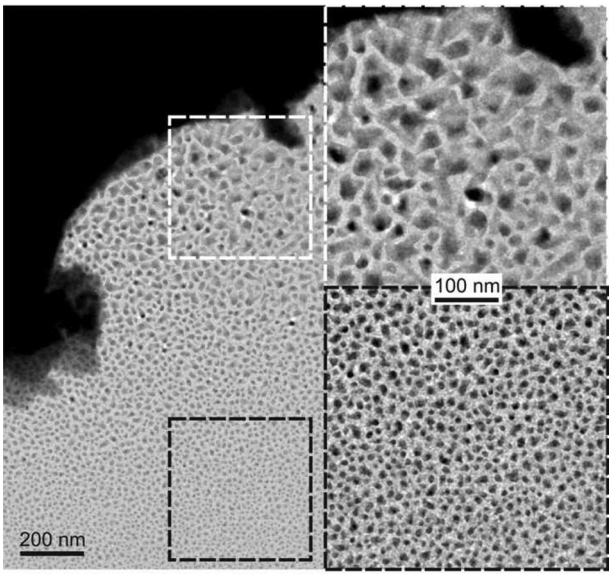

Figure 4. Bright field image of a particle of **X** after massive electron beam impact with enlarged sections showing the characteristic particle size distribution next (top) and apart the particle edge (bottom).

According to electron diffraction and HRTEM, all of the particles formed by electron beam impact are crystalline; however, EDX data indicates strong fluctuations of the composition, particularly concerning the In:S ratio. Moreover, the presence of faceted and non-faceted nanoparticles suggests a separation into distinct species.

The faceted crystals (e.g. Figure 5a) were determined as binary phases In-S, which show electron diffraction patterns that can be assigned to the spinel-type α-In_2S_3. The non-faceted particles were identified as pure indium, cf. FFT in Figure 5b for a particle aligned in zone axis orientation [111] (d(101) = 2.75 Å, d(110) = 2.32 Å, calculated values based on [29]:

Zeitschrift für anorganische und allgemeine Chemie ZAAC Journal of Inorganic and General Chemistry

2.72 Å, 2.30 Å). Additionally, EDX data prove the increase of the indium content, as evidenced by the spectra recorded on point 3 marked in Figure 6.

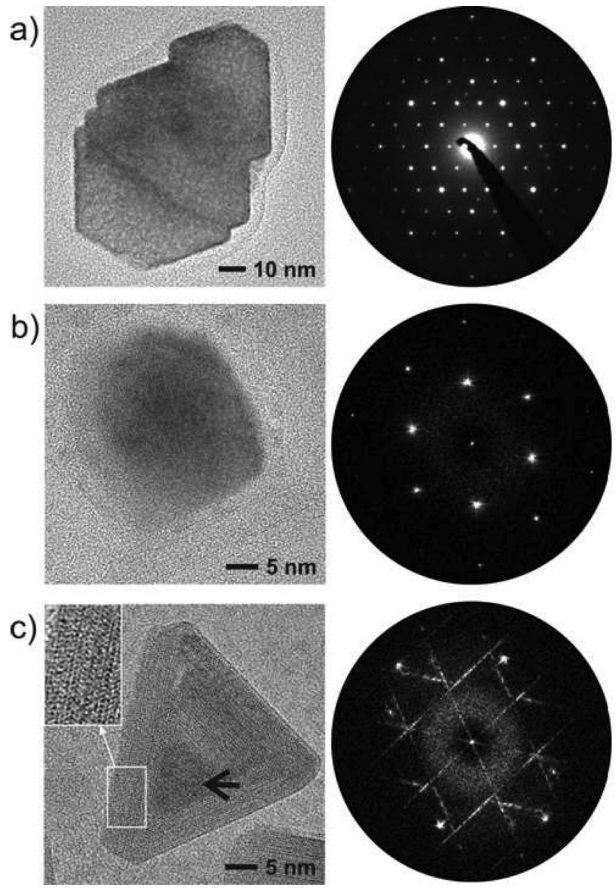

Figure 5. a) Bright field image of a crystal of α-In_2S_3 with electron diffraction pattern (both zone axis [110]); b) Indium nanoparticle with FFT of the image, zone axis [111]; c) Core-shell structure with a crystalline core of indium and shells of an indium sulfide. Inserted: enlarged section, see marks, attached FFT of the image.

Interestingly, the ratio In:S of the sulfur containing species is frequently found to be larger than one which is in contradiction with the nominal composition known for crystalline In-S phases (note that the phase described as "In_5S_4" [37] is truly $SnIn_4S_4$ [38]). This discrepancy is rationalized by a core-shell morphology made by indium (core) and a binary In-S phase (shell), respectively. The shape of the shell resembles simple polygons folded around the core; see for instance the triangular shape depicted in Figure 5c. However, the cores frequently take off-center positions as demonstrated by the enlarged section in Figure 6, bottom. The atomic structure of the shells is characterized by prominent disorder of layered structural motifs as can bee seen in the enlarged section in Figure 5c. Thus, the FFTs calculated inside square areas of the shell exhibit lines of diffuse intensity, and the complete FFT contains a set of parallel lines. The pattern formed by the diffuse lines depends on the overall shape of the shell, cf. hexagonal diffuse pattern from the triangular particle in Figure 5c. Spatially resolved nanoprobe-EDX analyses on the core and the shell do

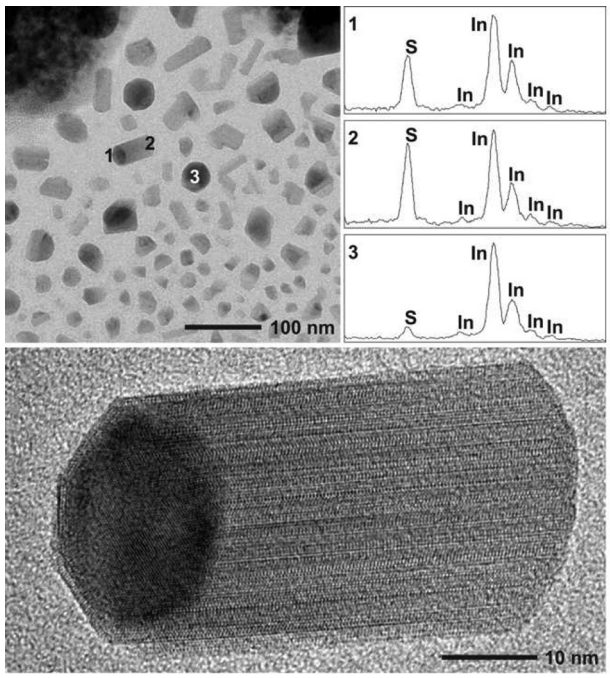

Figure 6. EDX performed on the composite **RP10**. It consists of particles of indium and indium sulfide (points 1 and 2) and particles of indium (point 3, stray intensity from sulfur in the surrounding), see text. Bottom: enlarged view of the composite.

not separate the constituents due to their superposition. However, as illustrated in Figure 6 the quantification of the spectra recorded next to points 1 and 2 demonstrates the reversal of the In:S ratio, i.e. the ratio is larger and smaller than 1 when transmitting the core area (point 1: In:S ~ 1.33) and the shell (point 2: In:S ~ 0.85), respectively.

*3.2.2 Sample Obtained After Rapid Pyrolysis for 5 s (**RP5**)*

When annealing the pristine material rapidly for five seconds, **W** and **X** still represent the major components, and again **X** can be decomposed by the in-situ evaporation experiment with the results described above (the evaporation of core-shell nanocrystals). Moreover, a third component (**Y**) can be identified forming aggregates of amorphous nanoparticles, cf. Figure 7. The EDX analyses (four point measurements) indicate an atomic ratio of Cu:In:S = 3.56 (3):34.36 (24):62.08 (20) and the presence of larger amounts of carbon, maybe produced by the decomposition of the precursor material. Note that according to the EDX data the copper content of **Y** with respect to **X** is decreased.

The amorphous structure is well seen in the enlarged section of Figure 7 and in the attached electron diffraction pattern which was recorded inside a selected area containing only amorphous material. The broad rings with diffuse intensity could represent the most prominent two-body correlations of graphitic carbon; however, related diffraction patterns can also be expected for amorphous In_2S_3. In the latter case the diameter of the rings of 3.18 Å and 1.89 Å would correlate with the

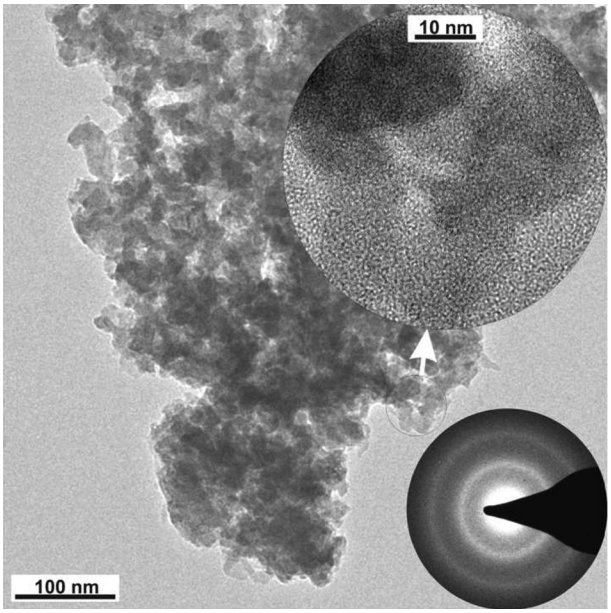

Figure 7. Aggregates of amorphous nanoparticles (component **Y**) after rapid thermal decomposition for five seconds. Bright field image with enlarged cutout and electron diffraction pattern.

values expected for the crystalline structure of α-In_2S_3 of d(311) and d(440) with 3.25 Å and 1.90 Å, respectively [29].

*3.2.3 Sample Obtained After Rapid Pyrolysis for 10 s (**RP10**)*

After 10 s of thermal annealing, all components were found to be crystalline. Larger particles (**Z1**) of micron size coexist with nanocrystals (**Z2**) (see Figure 8a). Diffraction patterns recorded inside selected areas containing both species can be indexed assuming a spinel-type structure with the metrics reported for cubic α-In_2S_3, as specified in Figure 8. This finding suggests that both species are crystallizing in this structure type.

The chemical compositions of the species show significant fluctuations as indicated by large values of the variances, however, as a clear trend the copper content of **Z2** (Cu:In:S = 4:35:61) was found to be larger than for **Z1** (Cu:In:S = 1:38:61). Normalizing to the sulfur content, the empirical formulas of **Z1** and **Z2** are $Cu_{0.05}In_{1.87}S_3$ and $Cu_{0.2}In_{1.73}S_3$ respectively, thus the compounds are non-stoichiometric indium sulfides with composition close to In_2S_3. This gives an additional evidence to confirm that the structure of these compounds is cubic (α-In_2S_3), as reported in [32]. Note, that the low copper content does not change the lattice parameters with respect to pure α-In_2S_3 in a way which can be identified by electron diffraction. Actually, the structure of **Z2** can be characterized by focusing on aggregates or isolated nanoparticles. In this case, the electron diffraction patterns and FFTs match with those expected for the cubic spinel-type structure of α-In_2S_3. For instance, the particle in the center of Figure 8b is oriented close to zone axis [110] as proven by the *d* values determined from the FFT.

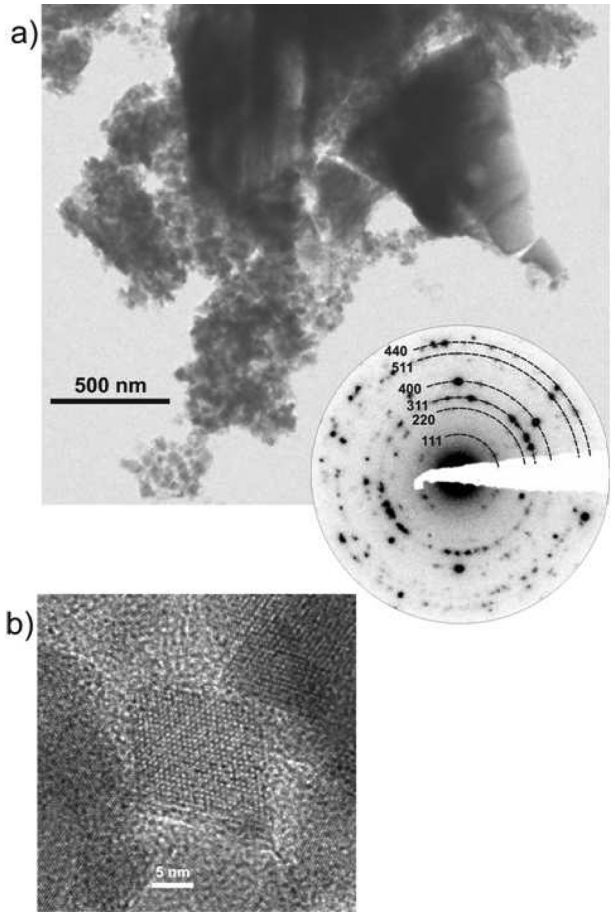

Figure 8. Large crystallites and nanoparticles (component **Z1** and **Z2**, respectively) of a ternary phase Cu-In-S. a) Bright field image with attached diffraction pattern recorded on a selected area containing **Z1** and **Z2**, and b) enlarged section showing a faceted nanoparticle of Cu-In-S (spinel-type, zone axis close to [110]).

With the aid of tilting experiments and HRTEM, the single crystalline particles of **Z1** can be assigned to the cubic spinel-type structure too. The diffracted intensity convincingly matches the calculated one, particularly when selecting the precession mode instead of the fixed beam mode, cf. Figure 9.

The HRTEM micrographs of Figure 10 were recorded close to the thin edge of a particle in the zone axis orientation [110]. The experimentally observed contrasts are well reflected by those of the inserted simulated micrographs, even for strong underfocus conditions, e.g. $\Delta f = -130$ nm (Figure 10, bottom). In case of $\Delta f = -45$ nm the imaging conditions of the Scherzer focus are approximated, i.e. the black spots represent high values of the projected potential and thus correlate with the indium atoms. For the simulation a spinel structure model with the lattice parameter of α-In_2S_3 was used and copper atoms were placed on the empty sites like in the structure of $CuIn_5S_8$.

3.3 UV/Vis Spectroscopy

The optical band gap E_g of the sample **RP10** was determined applying the Kubelka–Munk method using the UV/Vis reflec-

Zeitschrift für anorganische und allgemeine Chemie ZAAC Journal of Inorganic and General Chemistry

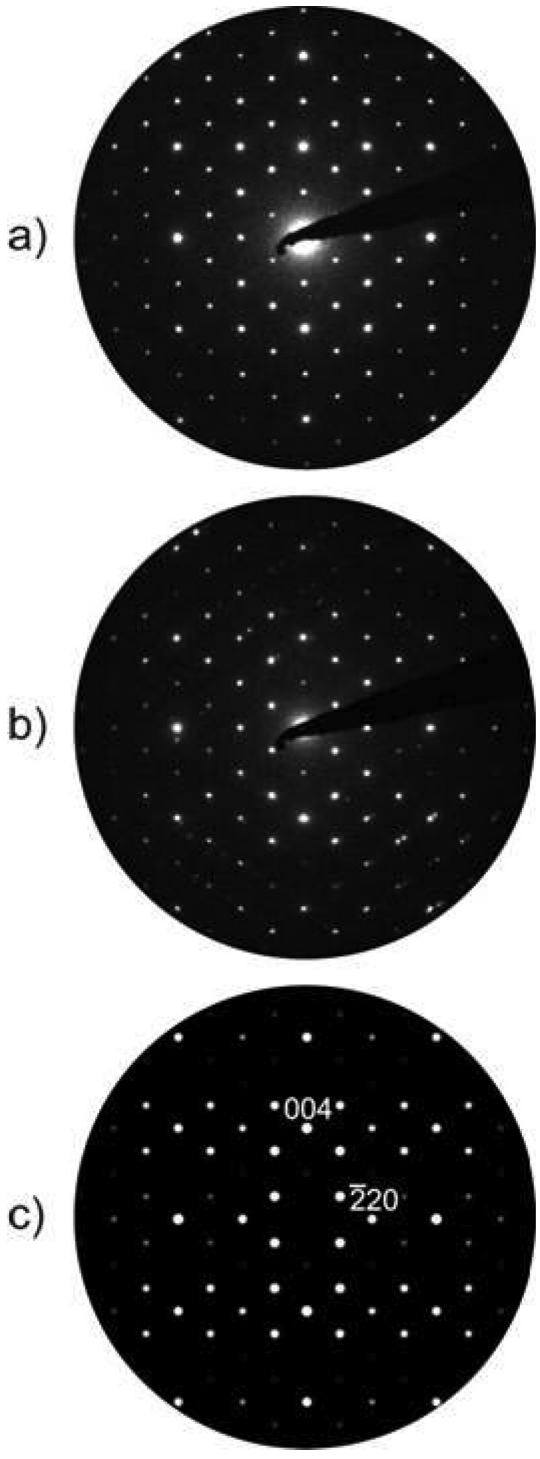

Figure 9. SAED (a) and PED (b) pattern recorded on component **Z1**, c) simulated PED pattern (precession angle: 3°, thickness 30 nm) based on the structure of α-In_2S_3, zone axis [110].

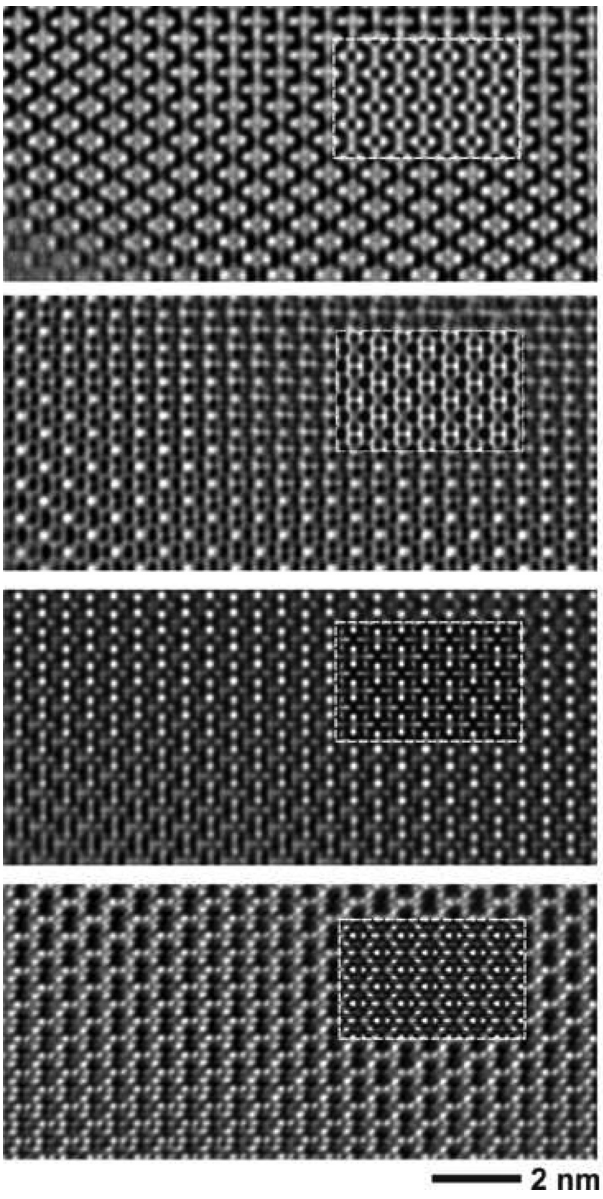

Figure 10. HRTEM performed on component **Z1**. Zone axis [110], parameters for inserted simulated micrographs: Thickness: 6 nm, and relative defocus values (from top to bottom): Δf = +5 nm, Δf = –45 nm, Δf = –85 nm, Δf = –130 nm.

tance spectrum of a powdered sample. For this purpose α^2/s^2 is plotted against the energy, with α being the absorption coefficient and s the scattering coefficient [39]. In the Kubelka–Munk plot for **RP10** two absorption steps with edge energies at 1.3 eV and 2.2 eV can be identified (Figure 11). These values are close to the corresponding E_g of single crystals of $CuIn_5S_8$ (1.31 eV) [40] and β-In_2S_3 (2 eV) [41].

It was reported that doping β-In_2S_3 with different amounts of copper allows tuning E_g between these two values [42]. In **RP10** the band gap of 1.3 eV can be due to the component with larger copper content (**Z2**) and the band gap of 2.2 eV should correspond to the one with less copper content (**Z1**). The small peak in the spectrum around 1.45 eV is due to the change of detector in this region.

3.4 Raman Spectroscopy

The Raman spectrum measured for the sample **RP10** can be deconvoluted in four bands that have maxima at 306, 322, 340

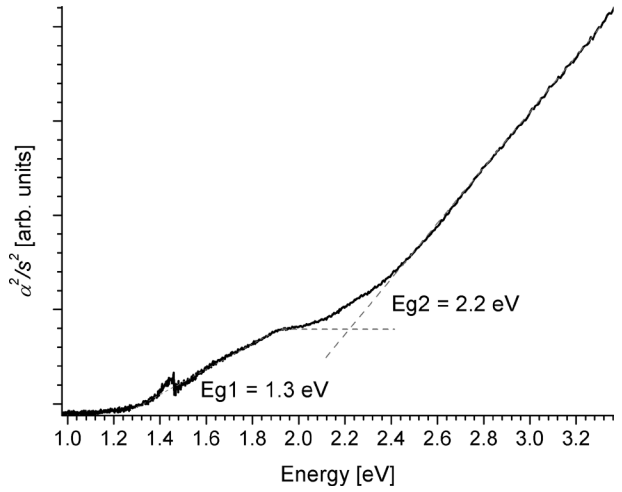

Figure 11. Kubelka–Munk plot for the determination of the optical band-gap of **RP10**. The steps at 1.3 and 2.2 eV correspond to the band-gaps of **Z2** and **Z1** respectively.

and 357 cm^{-1}, as shown in Figure 12. In this range β-In_2S_3 presents three Raman bands with peaks at 306, 326 and 367 cm^{-1} [43]. There are no reports of the Raman spectrum of α-In_2S_3, nevertheless according to the group theory it should be very similar to the one of β-In_2S_3. In fact, when analyzing the infrared spectra of α- and β-In_2S_3 one can not distinguish a marked difference [43, 44]. Additionally the infrared- and Raman-active modes of β-In_2S_3 at the centre of the Brillouin zone occur in the same range of frequencies, which is relatively narrow, but the differences in frequencies between infrared- and Raman-active modes is sufficiently large to consider that the principle of complementarity is obeyed: modes active in infrared are Raman-inactive [43]. In this way one can assume that the Raman spectra of α- and β-In_2S_3 are very similar. The peaks of **RP10** fit very well with the peaks of In_2S_3; just the peak at around 340 cm^{-1} does not correspond to this material.

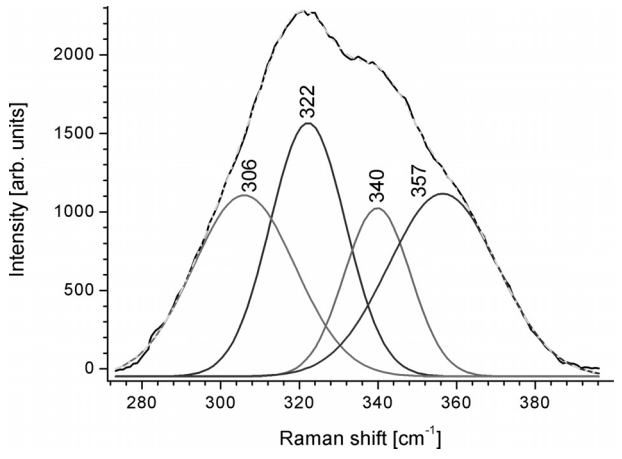

Figure 12. Raman spectrum of **RP10**. The three deconvoluted bands with peaks at 306, 322 and 357 cm^{-1} fit with the peaks of In_2S_3, and the peak at 340 cm^{-1} is related with interstitial copper in the compound.

The additional peak may be caused by the copper atoms occupying the sites that are normally empty in α-In_2S_3. Actually, $CuIn_5S_8$, with cubic structure very similar to α-In_2S_3, exhibits a resonance in the position of the additional peak at around 340 cm^{-1} [45, 46]. The broadness of the Raman peaks of **RP10** is due to the nanocrystalline nature of the material.

4 Conclusions

The thermal decomposition of $(C_{13}H_{28}N_2)_5[Cu_2In_{18}S_{33}]\cdot xH_2O$ at small time scales at elevated temperature yields a complex mixture of compounds with varying Cu:In:S ratios. The similarity of the X-ray diffraction patterns of the known modifications of In_2S_3 and $CuIn_5S_8$ complicates the assignment of distinct phases when analyzing the samples by X-ray powder diffraction. Electron microscopy evidences the presence of two distinct crystalline phases both crystallizing in the cubic spinel-type structure. The main difference between these components is the Cu:In:S ratio. Their compositions determined with EDX suggest the presence of ternary cubic copper poor phases, i.e., one may view the compounds as copper-doped cubic In_2S_3 with approximately compositions $Cu_{0.2}In_{1.73}S_3$ and $Cu_{0.05}In_{1.87}S_3$. Both compounds are non-stoichiometric, which might be another hint to think that the symmetry of their structure is cubic. The optical band gaps determined by UV/Vis reflectance measurements of 1.3 and 2.2 eV clearly indicate a mixture of two phases. In-situ conversion by an intense electron beam bombardment of the precursor material and the one obtained after 5 s heat treatment transforms the materials to core-shell copper-doped In/α-In_2S_3 nanoparticles that are monodisperse at equivalent distances from the heating point.

Further experiments are under way for an optimization of the decomposition procedure in which the content of amorphous carbon is reduced and which lead to a homogeneous distribution of the elements over the nanocrystals.

Acknowledgement

The authors would like to thank *Prof. Dr. Dr. h. c. mult. A. Simon* from the Max Plank Institute for Solid State research for enabling the TEM experiments. The support of *CONACyT* and *DAAD* is also appreciated.

References

[1] D. K. Nagesha, X. Liang, A. A. Mamedov, G. Gainer, M. A. Eastman, M. Giersig, J. J. Song, T. Ni, N. A. Kotov, *J. Phys. Chem. B* **2001**, *105*, 7490.
[2] Y. Xing, H. Zhang, S. Song, J. Feng, Y. Lei, L. Zhao, M. Li, *Chem. Commun.* **2008**, 1476.
[3] R. Diehl, C. D. Carpentier, R. Nitsche, *Acta Crystallogr., Sect. B* **1976**, *32*, 1257.
[4] R. Diehl, R. Nitsche, *J. Cryst. Growth* **1973**, *20*, 38.
[5] N. Barreau, *Sol. Energy* **2009**, *83*, 363.
[6] R. Diehl, R. Nitsche, *J. Cryst. Growth* **1975**, *28*, 306.
[7] T. T. John, M. Mathew, C. S. Kartha, K. P. Vijayakumar, T. Abe, Y. Kashiwaba, *Sol. Energy Mater. Sol. Cells* **2005**, *89*, 27.
[8] N. Kamoun, S. Belgacem, M. Amlouk, R. Bennaceur, J. Bonnet, F. Touhari, M. Nouaoura, L. Lassabatere, *J. Appl. Phys.* **2001**, *89*, 2766.
[9] A. Darga, D. Mencaraglia, Z. Djebbour, A. Migan Dubois, R. Chouffot, J. Serhan, F. Couzinié-Devy, N. Barreau, J. Kessler, *Thin Solid Films* **2009**, *517*, 2423.

[10] B. Asenjo, A. M. Chaparro, M. T. Gutiérrez, J. Herrero, J. Klaer, *Thin Solid Films* **2009**, *515*, 6036.
[11] S. Spiering, L. Bürkert, D. Hariskos, M. Powalla, B. Dimmler, C. Giesen, M. Heuken, *Thin Solid Films* **2009**, *517*, 2328.
[12] B. Asenjo, C. Sanz, C. Guillén, A. M. Chaparro, M. T. Gutiérrez, J. Herrero, *Thin Solid Films* **2007**, *515*, 6041.
[13] S. Buecheler, D. Corica, D. Guettler, A. Chirila, R. Verma, U. Müller, T. P. Niesen, J. Palm, A. N. Tiwari, *Thin Solid Films* **2009**, *517*, 2312.
[14] W. Chen, J. O. Bovin, A. G. Joly, S. Wang, F. Su, G. Li, *J. Phys. Chem. B* **2004**, *108*, 11927.
[15] G. Cao, Y. Zhao, Z. Wu, *J. Alloys Compd.* **2009**, *472*, 325.
[16] X. Cao, L. Gu, L. Zhuge, W. Qian, C. Zhao, X. Lan, W. Sheng, D. Yao, *Colloids Surf. A: Physicochem. Eng. Aspects* **2007**, *297*, 183.
[17] R. Jayakrishnan, T. T. John, C. S. Kartha, K. P. Vijayakumar, T. Abe, Y. Kashiwaba, *Semicond. Sci. Technol.* **2005**, *20*, 1162.
[18] Y. He, D. Li, G. Xiao, W. Chen, Y. Chen, M. Sun, H. Huang, X. Fu, *J. Phys. Chem. C* **2009**, *113*, 5254.
[19] Y. Xiong, Y. Xie, G. Du, X. Tian, *J. Mater. Chem.* **2002**, *12*, 98.
[20] D. P. Dutta, G. Sharma, A. K. Tyagi, S. K. Kulshreshtha, *Mater. Sci. Eng. B* **2007**, *138*, 60.
[21] S. H. Choe, T. H. Bang, N. O. Kim, H. G. Kim, C. I. Lee, M. S. Jin, S. K. Oh, W. T. Kim, *Semicond. Sci. Technol.* **2001**, *16*, 98.
[22] J. Tang, G. Konstantatos, S. Hinds, S. Myrskog, A. G. Pattantyus-Abraham, J. Clifford, E. H. Sargent, *ACS Nano* **2009**, *3*, 331.
[23] T. C. Deivaraj, J. H. Park, M. Afzaal, P. O'Brien, J. J. Vittal, *Chem. Mater.* **2003**, *15*, 2383.
[24] M. Calixto Rodriguez, H. Martínez, A. Sanchez Juarez, *Thin Solid Films* **2009**, *517*, 2332.
[25] P. Feng, X. Bu, N. Zheng, *Acc. Chem. Res.* **2005**, *38*, 293.
[26] C. Wang, Y. Li, X. Bu, N. Zheng, O. Zivkovic, C. S. Yang, P. Feng, *J. Am. Chem. Soc.* **2001**, *123*, 11506.
[27] R. Vincent, P. A. Midgley, *Ultramicroscopy* **1994**, *53*, 271.
[28] T. E. Weirich, J. Portillo, G. Cox, H. Hibst, S. Nicolopoulos, *Ultramicroscopy* **2006**, *106*, 164.
[29] H. E. Swanson, R. K. Fuyat, *J. Less-Com. Met.* **1964**, *7*, 17.
[30] G. A. Steigmann, H. H. Sutherland, J. Goodyear, *Acta Crystallogr.* **1965**, *19*, 967.
[31] J. Morales, J. L. Tirado, M. L. Eldrissi Moubtassim, J. Olivier-Fourcade, J. C. Jumas, *Rev. Chim. Min.* **1987**, *24*, 10.
[32] A. Likforman, M. Guittard, A. Tomas, J. Flahaut, *J. Solid State Chem.* **1980**, *34*, 353.
[33] N. Barreau, C. Deudon, A. Lafond, S. Gall, J. Kessler, *Sol. Energy Mater. Sol. Cells* **2006**, *90*, 1840.
[34] N. Barreau, J. C. Bernède, C. Deudon, L. Brohan, S. Marsillac, *J. Cryst. Growth* **2002**, *241*, 4.
[35] B. J. Kooi, W. M. G. Groot, J. T. M. de Hosson, *J. Appl. Phys.* **2004**, *95*, 924.
[36] A. Leen Koh, K. Bao, I. Khan, W. E. Smith, G. Kothleitner, P. Nordlander, S. A. Maier, D. W. McComb, *ACS Nano* **2009**, *3*, 3015.
[37] T. Wadsten, L. Arnberg, J. E. Berg, *Acta Crystallogr., Sect. B* **1980**, *36*, 2220.
[38] H. J. Deiseroth, H. Pfeifer, *Z. Kristallogr.* **1991**, *196*, 197.
[39] D. Gal, Y. Mastai, G. Hodes, *J. Appl. Phys.* **1999**, *86*, 37.
[40] A. F. Qasrawi, N. M. Gasanly, *Cryst. Res. Technol.* **2003**, *38*, 1063.
[41] W. Rehwald, G. Harbeke, *J. Phys. Chem. Solids* **1965**, *26*, 1309.
[42] N. Barreau, J. C. Bernède, J. Kessler, in: *19th European Photovoltaic Solar Energy Conference*, **2004**, p. 223.
[43] K. Kambas, J. Spyridelis, M. Balkanski, *Phys. Status Solidi B* **1981**, *105*, 291.
[44] I. V. Bodnar, A. G. Karoza, E. A. Kudritskaya, A. G. Smirnova, *J. Appl. Spectrosc.* **1997**, *64*, 279.
[45] J. Álvarez-García, A. Pérez-Rodríguez, A. Romano-Rodríguez, J. R. Morante, *J. Vac. Sci. Technol. A* **2001**, *19*, 232.
[46] N. M. Gasanly, S. A. El-Hamid, L. G. Gasanova, A. Z. Magomedov, *Phys. Status Solidi B* **1992**, *169*, K115.

Received: March 10, 2010
Published Online: June 29, 2010

